



# MHD Simulation of a Solar Eruption from Active Region 11429 Driven by a Photospheric Velocity Field

Xinyi Wang<sup>1,2</sup> , Chaowei Jiang<sup>3</sup> , and Xueshang Feng<sup>1,3</sup>

<sup>1</sup> SIGMA Weather Group, State Key Laboratory for Space Weather, National Space Science Center, Chinese Academy of Sciences, Beijing 100190, People's Republic of China

<sup>2</sup> College of Earth and Planetary Sciences, University of Chinese Academy of Sciences, Beijing 100049, People's Republic of China

<sup>3</sup> Institute of Space Science and Applied Technology, Harbin Institute of Technology, Shenzhen 518055, People's Republic of China; [chaowei@hit.edu.cn](mailto:chaowei@hit.edu.cn)

Received 2022 November 13; revised 2022 December 22; accepted 2022 December 23; published 2023 January 17

## Abstract

Data-driven simulation is becoming an important approach for realistically characterizing the configuration and evolution of solar active regions, revealing the onset mechanism of solar eruption events, and hopefully achieving the goal of accurate space weather forecasting, which is beyond the scope of any existing theoretical modeling. Here we performed a full 3D MHD simulation using the data-driven approach and followed the whole evolution process from the quasi-static phase to eruption successfully for solar active region (AR) NOAA 11429. The MHD system was driven at the bottom boundary by a photospheric velocity field, which is derived by the DAVE4VM method from the observed vector magnetograms. The simulation shows that a magnetic flux rope was generated by a persistent photospheric flow before the flare onset and then triggered to erupt by torus instability. Our simulation demonstrates a high degree of consistency with observations in the preeruption magnetic structure, the timescale of the quasi-static stage, the pattern of flare ribbons, as well as the time evolution of the magnetic energy injection and total unsigned magnetic flux. We further found that an eruption can also be initiated in the simulation driven by only the horizontal components of the photospheric flow, but a comparison of the different simulations indicates that the vertical flow at the bottom boundary is necessary for reproducing more realistically these observed features, emphasizing the importance of flux emergence during the development of this AR.

*Unified Astronomy Thesaurus concepts:* Solar coronal mass ejections (310); Solar flares (1496); Solar active region magnetic fields (1975); Magnetohydrodynamics (1964); Magnetohydrodynamical simulations (1966)

*Supporting material:* animation

## 1. Introduction

Driven by solar eruptions, the solar-terrestrial environment often experiences variations, which are known as space weather, and forecasting space weather precisely is not only an important scientific topic but also can help in avoiding damage to sensitive critical on-ground and space-based infrastructures. Though many theoretical models have been proposed and significant progress has been made in understanding the triggering mechanism of solar eruptions (Forbes 2000; Chen 2011; Schmieder et al. 2013; Priest 2014), reproducing the whole life span from the quasi-static stage to eruption using numerical models constrained and driven by observed vector magnetograms possess unprecedented capabilities in revealing the onset mechanism of real eruption events and can potentially be used for accurate space weather forecasting (Jiang 2022; Jiang et al. 2022).

A previous study has reproduced the entire process of energy accumulation and release successfully (Jiang et al. 2016), showing an MHD system can be driven to erupt by inputting time series of vector magnetograms at the bottom boundary ( $B$  driven). There are also other data-driven models in which the evolution of the MHD system is driven by the electric field ( $E$  driven; e.g., Cheung & DeRosa 2012; Hayashi et al. 2018; Price et al. 2019; Pomoell et al. 2019) or the velocity field ( $V$

driven; e.g., Guo et al. 2019; Hayashi et al. 2019; Liu et al. 2019; He et al. 2020; Zhong et al. 2021) on the photosphere (bottom boundary). Though the  $B$ -driven method can fully match the magnetogram, it will introduce considerable errors owing to magnetic divergence from the bottom boundary. This shortcoming vanishes in the  $E$ -driven model; however, deriving both the induction and potential components of the electric field on the photosphere is not an easy task (Fisher et al. 2010, 2012, 2015, 2020), and the photospheric flow also needs to be properly set to follow Ohm's law. In most theoretical models of solar eruption, the key structure in favor of eruption is assumed to be formed through the movement of the footpoints of magnetic field lines (Moore & Labonte 1980; Moore & Roumeliotis 1992; Antiochos et al. 1999; Lin & Forbes 2000; Jiang et al. 2021b), which is driven by the horizontal flow, and the vertical component of the photospheric flow will be responsible for the flux emergence process. Therefore, with the photospheric velocity field determined, the photospheric magnetic field can be generated self-consistently. Furthermore, in the  $V$ -driven approach, there is no need to solve the complex momentum equation at the bottom boundary (which is the most time-consuming part of solving MHD equations). Due to these advantages, the  $V$ -driven method has attracted many previous studies focusing on this topic. For example, with the velocity field derived by the DAVE4VM method (Schuck 2008), Hayashi et al. (2019) used the projected normal characteristics method to update the physical variables other than the velocity at the bottom boundary. However, the total magnetic energy was kept at almost the same level as that of the initial state without obvious magnetic energy injection.



Original content from this work may be used under the terms of the [Creative Commons Attribution 4.0 licence](https://creativecommons.org/licenses/by/4.0/). Any further distribution of this work must maintain attribution to the author(s) and the title of the work, journal citation and DOI.

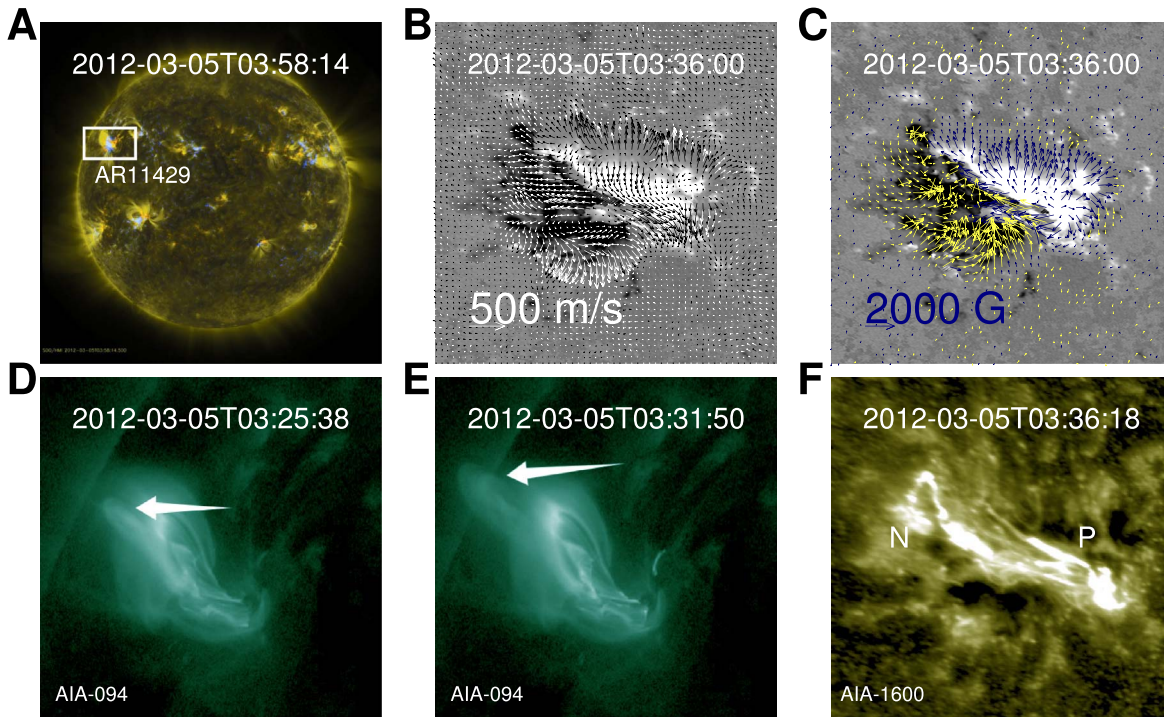


**Figure 1.** (A) A full-disk composite image of the SDO AIA 171 Å and HMI magnetogram. The white box shows the AR 11429. (B) The vectors denote the time-average horizontal velocity from 2012 March 4 00:00 UT to March 5 03:36 UT on the photosphere. The background shows the magnetic flux distribution, in which black and white represent the negative and positive polarities, respectively. (C) The vectors denote the transverse magnetic field on the photosphere. (D) Preflare image of AIA 94 Å. The white arrow shows the erupting structure. (E) Same as D, but at a time closer to eruption before the flare onset. (F) The first image of flare ribbons observed in AIA 1600 Å. Letter P labels the positive ribbon and N labels the negative ribbon.

Jiang et al. (2021a) updated the magnetic field by solving directly the magnetic induction equation at the bottom boundary, and their model can inject magnetic energy from the bottom boundary successfully. He et al. (2020) drove the magnetic evolution by inputting the DAVE4VM velocity field and vector magnetogram simultaneously. The formation process of a magnetic flux rope (MFR) was obtained in their model. Unfortunately, these simulations did not drive the system to erupt. The only work we know that obtained an eruption with the velocity field derived from observation was shown in Kaneko et al. (2021). The velocity field was derived from the electric field on the photosphere using Ohm’s law and then was inputted at the bottom boundary in their zero-beta model to drive the system to erupt. The two eruptions they produced were identified from the evolution curves of the magnetic and kinetic energies; however, the kinetic energy showed an overall increase without obvious quasi-static evolution during the preeruption stage. Before the first eruption, the kinetic energy was comparable with its peak during the first eruption and the amount of the magnetic energy released was also too small; it did not show the feature of a typical eruption event, i.e., a large amount of magnetic energy converted into kinetic energy impulsively. As described above, the whole energy accumulation process from quasi-static evolution (of typically tens of hours) to impulsive eruption has not been realized in a self-consistent way using the  $V$ -driven MHD model, and this is one of the motivations of this work.

In this Letter, we applied a  $V$ -driven model to investigate the evolution and eruption of a well-studied active region (AR), NOAA 11429. Previous studies found a persistent shearing flow and flux cancellation near the main polarity inversion line

(PIL) of this AR (Shimizu et al. 2014; Zheng et al. 2017), which were suggested to be responsible for the eruptions on 2012 March 7, 9, and 10 (Dhakal et al. 2018, 2020). An analysis of the MFR reconstructed from vector magnetograms using the nonlinear force-free field (NLFFF) model suggests that the homologous eruptions are triggered by the torus instability (TI) of the MFR (Chintzoglou et al. 2015). Zhang et al. (2021) suggested that helical kink instability may also take effect. Nevertheless, whether these mechanisms were at work requires further studies using dynamic modeling of this AR evolution and eruption, which is absent in all the previous studies and is the other motivation for this work. In our simulation, the dynamic process from the beginning of 2012 March 4 to the eruption on March 5 in this AR was reproduced self-consistently, driven by the photospheric velocity derived from vector magnetograms using the DAVE4VM method. Our simulation shows that an MFR was generated near the main PIL before the flare onset, and the initiation of this eruption event depended mainly on the TI of the preformed MFR.

## 2. Data and Model

AR 11429 showed a complex  $\beta\gamma\delta$  configuration and is very flare-productive, producing three X-class flares from 2012 March 5 to 7. It first appeared on the eastern solar limb on March 4 and was located on the eastern part of the solar disk before March 8. During this period, the AR kept developing, as characterized by the increasing total unsigned magnetic flux, indicating obvious flux emergence by the vertical flow on the photosphere. Since it was the first X-class flare of this AR, here we focus on the initiation process of the X1.1 flare (which is accompanied by a halo coronal mass ejection moving at a speed of  $1531 \text{ km s}^{-1}$ ) around 04:00 UT on March 5 as shown

in the white box in Figure 1(A). Before the flare onset, there was a persistent shearing flow near the main PIL (Figure 1(B)), and as a result, the horizontal magnetic field there was highly sheared (Figure 1(C)), which indicates that a large amount of free magnetic energy is stored, ready for an eruption. A hot loop first erupted as shown in AIA 94 Å (Lemen et al. 2012) at around 03:31 UT (Figures 1(D) and (E)) and after that, a pair of hook-shape flare ribbons appeared near the main PIL in AIA 1600 Å at 03:36 UT (Figure 1(F)), i.e., the flare event started.

To understand the formation of the preeruptive coronal magnetic field and the triggering mechanism of this eruption, we used the DARE-MHD model (Jiang et al. 2016) to study the dynamic evolution of this AR. To save computational time, the strength of the magnetic field from the magnetograms was reduced by a factor of 25 before being input into our code. The initial plasma density was set as a hydrostatic isothermal model with a fixed temperature of  $T = 1 \times 10^6$  K and a modified solar gravity (Jiang et al. 2021b) to get a plasma background that mimics the real environment in the solar corona based on two key parameters, the plasma  $\beta$  and the Alfvén speed (in particular, the minimum  $\beta$  is  $6.3 \times 10^{-4}$  and maximum Alfvén speed  $V_A \sim 4800$  km s $^{-1}$  in the final equilibrium we obtained below). We chose to use the magnetograms of the HMI SHARP data set (Schou et al. 2012; Bobra et al. 2014) at 00:00UT on March 4 to reconstruct the initial magnetic field since there was no obvious MFR at that time. This magnetogram was smoothed first using Gaussian smoothing with an FWHM of 6 pixels, and an NLFFF model from this smoothed magnetogram was extrapolated by our CESE-NLFFF-MHD code (Jiang & Feng 2012, 2013). Since the code (like many other NLFFF codes) does not give a perfect force-free solution but with residual Lorentz forces, we input the extrapolated field into the DARE-MHD model, along with the initial background plasma, to let the MHD system relax until the kinetic and magnetic energies were almost unchanged, i.e., an MHD equilibrium was obtained, and the initial state was ready.

At the bottom boundary, we solve the magnetic induction equation to update the magnetic field with the velocity field derived by the DAVE4VM method to update the magnetic field on the photosphere. The DAVE4VM velocity was strengthened by a factor of 13.7 (determined by the ratio of the time series magnetograms’ original time cadence of 720 s to the time cadence in our simulation of  $0.5 \times 10^5$  s, i.e.,  $\frac{720}{0.5 \times 10^5}$ ) to speed up our simulation, and thus, the timescale of quasi-static evolution prior to the eruption onset is shortened by the same times. At the side and top boundaries, all the variables are extrapolated from the neighboring inner points with zero gradient along the normal direction of the boundary surface, and the normal component of the magnetic field is further modified by the divergence-free condition. The Powell source terms and diffusion control terms were used to deal with the divergence error of the magnetic field as described in Jiang et al. (2010). We set the computational domain to be sufficiently large,  $[-368, 368]$  Mm, in both  $x$  and  $y$  directions and  $[0, 736]$  Mm in the  $z$  direction, with grid resolution varying from  $1''$  to  $8''$  using adaptive mesh refinement. The highest resolution is used mainly for the regions with strong magnetic gradients and current density, in particular, the current sheets (CSs). An explicit value of magnetic resistivity was not used in our simulation, and the magnetic reconnection was controlled by the resistivity of the numerical method only, which

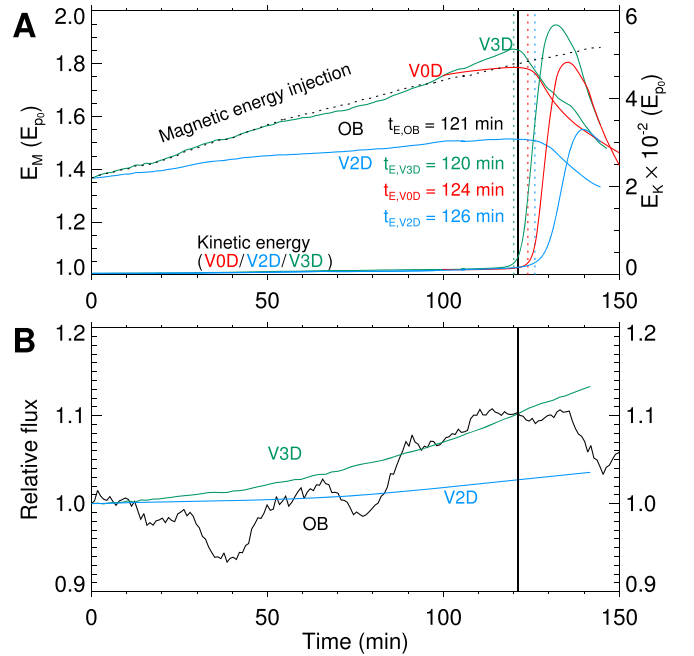


**Figure 2.** (A) Magnetic and kinetic energy evolution during the whole process. The unit of the  $x$ -axis is in minutes. The solid curves in different colors denote the corresponding evolution of different energies, and the vertical dashed lines in different colors denote the eruption onset time of different runs. The vertical black solid line shows the flare onset time in observations. The black curve “OB” denotes the magnetic energy injection computed by the DAVE4VM velocity and magnetograms, thus representing the actual magnetic energy evolution. In our simulation, the magnetic energy of the potential field of the initial magnetogram is  $E_{p0} = 2.52 \times 10^{30}$  erg (which is a fixed value and is used for normalization here). This value should be multiplied by a factor of  $625 = 25^2$  if scaling to the realistic value, thus being  $1.57 \times 10^{33}$  erg. (B) Time evolution of the total unsigned magnetic flux in our simulations. The “OB” curve is computed by the magnetograms and the other labels “V3D,” “V2D,” and the vertical black solid line have the same meanings as in (A). All curves are normalized by their initial value at  $t = 0$ . The corresponding animation is attached for the V3D run, and it starts at  $t = 0$  and ends at  $t = 147$  minutes in simulation time, which corresponds to 33.6 hr in real-time duration. Panel *a* in the animation corresponds to rows A in Figures 3 and 4. Panel *b* corresponds to rows C in Figures 3 and 4 in the time series. Panel *c* shows the corresponding evolution as in row D in Figure 4, and panel *d* represents the evolution of QSLs as in Figure 4(F). We only plotted the kinetic energy in panel *e*, with the vertical solid line showing the current simulation time; magnetic flux evolution is not included in the animation. The cadence between each snapshot used in the animation is 210 s in the quasi-static period ( $t \in [0, 119]$  minutes) and 21 s in the eruption period ( $t \in [119, 147]$  minutes) in simulation time, respectively. (An animation of this figure is available.)

mimicked the low-resistivity plasma better. As the total unsigned flux of this AR kept increasing before the flare onset, we energized the MHD system by the full 3D DAVE4VM velocity field ( $v_x^D, v_y^D, v_z^D$ ) (which will be referred to as the V3D simulation) and the horizontal component ( $v_x^D, v_y^D, 0$ ) (V2D), respectively, and a comparison of the results for these two simulations will show the importance of flux emergence through the vertical flow on the photosphere.

### 3. Results

#### 3.1. Overall Process

The evolution curves of the total magnetic and kinetic energies in the computational domain as well as the total unsigned magnetic flux at the bottom boundary are shown in Figure 2. For the “V3D” simulation, driven by the time-series velocity field (V3D) for a time duration of 150 minutes, the



total magnetic energy in our simulation model experienced an overall increase first and then a rapid decrease, which is associated with an eruption event. The eruption can be identified from the energy evolution with onset time  $t_{E,V3D} = 120$  minutes.

At the very beginning from  $t=0$  to  $t=22$  minutes, the magnetic energy injection curve (black dashed line; which is computed by the time integration of the total Poynting flux of the “V3D” simulation at the bottom surface) matches well with the solid “V3D” curve (the magnetic energy increase of the “V3D” simulation) and “OB” curve (the magnetic energy injection computed by the DAVE4VM velocity and magnetograms) in Figure 2(A). However, in the time duration of  $t \in [97, 122]$  minutes, the total magnetic energy (blue solid line) is higher than the magnetic energy injection. Such an unphysical mismatch of the inputted energy from the boundary and the cumulative energy in the volume likely owes to the insufficient resolution for the bottom boundary, since the magnetic field at the bottom boundary has accumulated a very large gradient in this phase (see Discussions). The kinetic energy remains at a very low value of around  $10^{-3}E_{p_0}$  (which is the potential field energy corresponding to the magnetic field at  $t=0$ ) before the major eruption begins at  $t_{E,V3D} = 120$  minutes when the magnetic energy reaches about  $1.85 E_{p_0}$ . The magnetic energy decreases to about  $1.7 E_{p_0}$  at the peak of the total kinetic energy (i.e.,  $E_k = 5.6 \times 10^{-2}E_{p_0}$ ) and keeps decreasing to  $1.45 E_{p_0}$  in total through this eruption ( $0.4 E_{p_0}$  free energy loss). That is, about one-third of the magnetic energy loss has been converted to kinetic energy in 10 minutes. If multiplied by a factor of 13.7 determined by the rate of speeding up in our velocity-driven simulation, the quasi-static evolution time of the “V3D” run is 27.4 hr. This timescale is very close to the observation one, which is 27.6 hr.

We have also driven the simulation with the horizontal velocity (V2D) and found that it can also produce an eruption with a rather similar onset time. However, comparing the different curves of the magnetic energy evolution in Figure 2(A) and the curves of the total unsigned magnetic flux in Figure 2(B), the blue solid lines labeled “V2D” are obviously lower than those from the “V3D” simulation. This clearly shows that though horizontal velocity can also drive the field to erupt (with a delayed onset time of about 6 minutes compared with “V3D”), the vertical velocity  $v_z^D$  is necessary to account for the larger increase of the total magnetic energy and total unsigned flux as shown in observations, therefore leading to a stronger eruption. The evolution of the simulated magnetic energy, total unsigned flux, and the timescale of the “V3D” run before the major eruption is more consistent with observations, showing the importance of the vertical photospheric plasma flow in the numerical modeling of solar eruptions. Our simulated magnetic structure (the first panel in Figure 3(E)) has reasonable consistency with observations in the preeruption image of AIA 171 Å (the second panel in Figure 3(E)), and the synthetic image of coronal emission from the current density of our simulation (the last panel in Figure 3(E)) is reasonably consistent with the image of AIA 131 Å (the third panel in Figure 3(E)). Also, the quasi-separatrix layers (QSLs), where the magnetic reconnection is most likely to take place and thus represent the position of the flare ribbons (Titov et al. 2002; Liu et al. 2016), at the bottom boundary (Figure 4(F)), have approximately the same patterns as the flare ribbons in AIA 1600 Å (Figure 4(E)). These results confirm the validity of our

V-driven DARE-MHD model as well as the DAVE4VM method.

### 3.2. Eruption Initiation Mechanism

Since the actual velocity field must contain  $v_z$ , here we analyzed the “V3D” run to study the onset mechanism of this eruption. As we can see, a group of twisted field lines (represented by the blue solid lines in Figures 3(A) and (B)) formed and was embedded in the surrounding shear arcades, which is similar to an MFR in morphology. In addition, the ejection of the hot loop (also called a hot channel) as observed in AIA 94 Å (shown by the white arrows in Figures 1(D) and (E)) also suggested the existence of an MFR (Cheng et al. 2017) before the flare onset.

To identify the formation of an MFR before eruption, we calculated the QSLs and the twist number (Berger & Prior 2006) of our simulated magnetic fields, which are given in Figure 3(D) and Figures 5(A) and (B), respectively. As shown in the third panel of Figure 3(D), a strong QSL appeared near the core field and grew to be a QSL ring in the last panel, separating the MFR and the background magnetic field, thus representing the existence of an MFR in topology. The QSL ring intersects itself below the MFR, forming a typical hyperbolic flux tube (HFT), where the CS developed and magnetic reconnection took place subsequently to further drive the eruption (Jiang et al. 2018). The isosurface of  $T_w = -1$ , which represents the position and shape of the MFR, is shown in Figures 5(A) and (B) respectively. It became larger and higher, illustrating more magnetic flux was twisted as driven by the persistent photospheric flow. However, the isosurface of  $T_w = -2$ , which is the lower threshold of kink instability (KI) according to the statistics of Duan et al. (2019), is barely visible and KI may have little effect.

Among different triggering mechanisms, TI is considered an efficient way for MFR eruption. In Figure 5(D), we plot the key controlling parameter that determines the onset of TI, i.e., the decay index of the strapping field. The variation of the decay index  $n$  was calculated along the  $z$  direction of the overlying field at  $t=119$  minutes before the eruption onset. Since the potential field is not always a good approximation of the strapping field (especially when the strapping field is highly sheared), we calculated the decay index of our simulated field instead and plotted the decay index of the corresponding potential field at the same time for comparison. The critical height (above which  $n > 1.5$ ) of the simulated field is located at 60 Mm as labeled by the vertical black dashed line in Figure 5(D). When the MFR was just formed, it is small and its apex was at a low height (about 40 Mm in Figure 5(A)). About 14 minutes later, it had grown up to be a huge twist structure and entered the unstable zone (above 60 Mm as shown in Figure 5(B)), after which it erupted violently.

The formation and the evolution of the MFR, i.e., there was a preformed MFR and the MFR erupted after it entered the unstable zone, strongly suggest that TI is the triggering mechanism of this eruption. To further test this assumption, we used the V3D-driven data at  $t=100$  minutes as the initial condition and ran our code without bottom velocity driven (by setting all three velocity components to zero at the bottom boundary, thus referred to as “V0D”) to see whether the magnetic field will erupt. The evolution of energies of this “V0D” run is shown as the red solid lines in Figure 2(A). During the time duration of  $t \in [100, 124]$  minutes, the

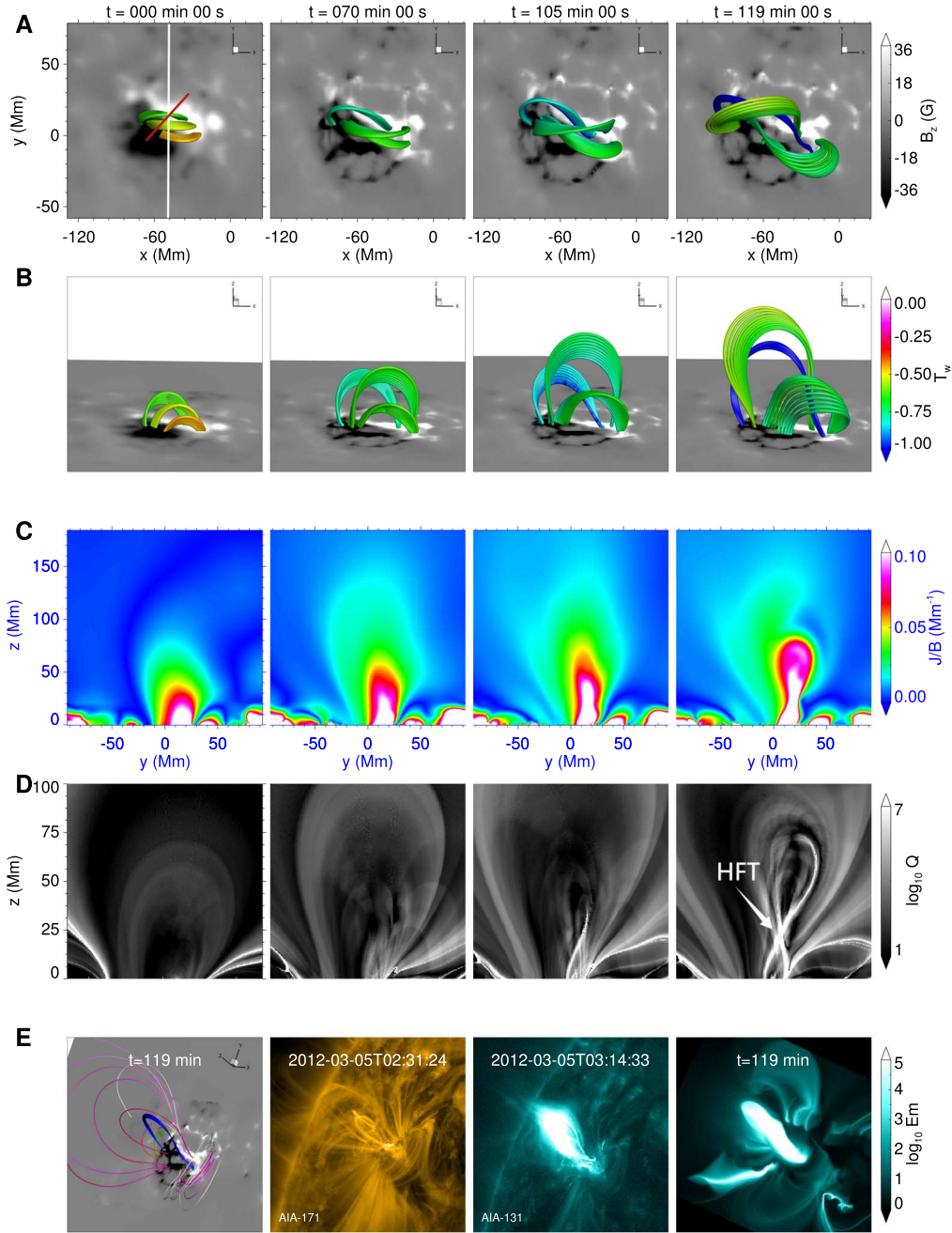


**Figure 3.** The magnetic evolution during the preeruption stage. (A) Top view of three bunches of field lines with the footpoints approximately following the movement of the magnetic flux. The white solid line denotes the position of the slices in C and in Figures 4(C) and (D). The red solid line segment shows the position of the slices in D, which is almost perpendicular to the PIL and at the middle of the MFR. (B) Side view of the same 3D magnetic field lines as in (A). (C) Vertical cross section of the current layer near the main PIL. The position of these slices is labeled by the white solid line in (A). (D) Magnetic squashing factor  $Q$  on the same cross section of C and the region with high  $Q$  denotes the QSLs. The position of these slices is labeled by the red solid line segment in (A). (E) The first two panels show the comparison between our simulation and observations in AIA 171 Å. The last two panels show a comparison between the synthetic image of coronal emission from the current density of our simulation and observations in AIA 131 Å. Row A is shown in panel *a*, and row C is shown in panel *c* in the animation of Figure 2, respectively.

magnetic energy remained almost unchanged, while the toroidal flux of the MFR (defined as  $\int_s B_z ds$ , where  $s$  denotes the region of  $T_w < -1$  and  $B_z < 0$  at the bottom boundary) kept increasing as shown in Figure 5(C). In the “V3D” simulation, the MFR (the isosurface of  $T_w = -1$ ) became larger and higher than the critical height before the eruption onset (Figures 5(A) and (B)) as the toroidal flux increased (Figure 5(C)), after which TI took effect and finally led to a strong eruption. Similarly, the toroidal flux of the “VOD” simulation increased

before and decreased after the eruption (Figure 5(C)), showing that slow reconnection can take place spontaneously without velocity driving and make the MFR larger until the eruption started at  $t_{E,VOD} = 124$  minutes as identified from the energy evolution curve. Since the current density was weaker and the current layer was thicker (as shown in the third panel in Figure 3(C)) than a true CS (the first panel in Figure 4(C)), the magnetic gradient was lower in the current layer than in the CS, and thus the diffusivity was relatively uniform, which only

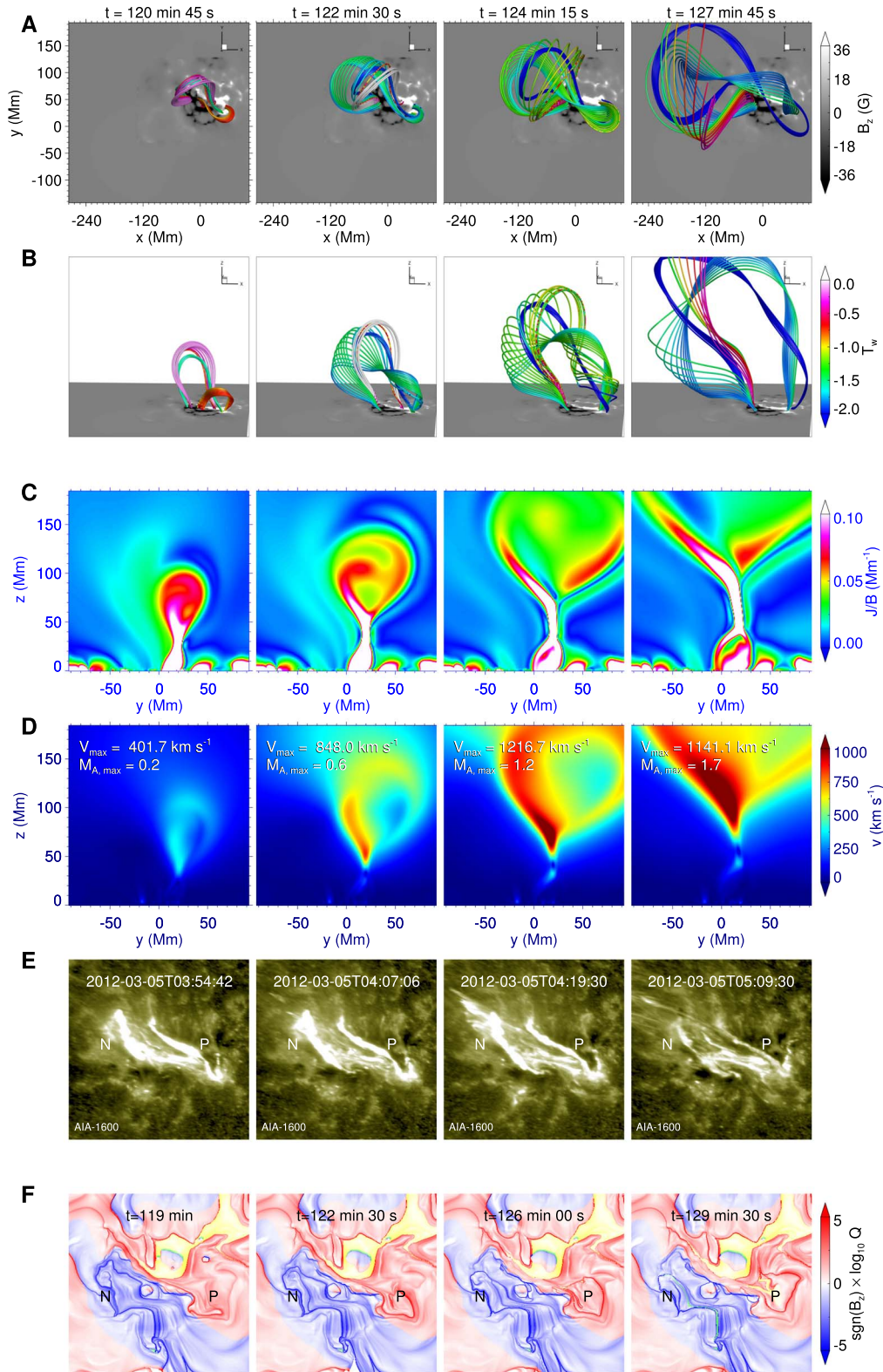


**Figure 4.** The magnetic evolution of the eruption stage. (A), (B), and (C) All settings are the same as in Figures 3(A), (B), and (C), except the footpoints of the magnetic field lines are fixed and the current layer in Figure 3(C) turns into a current sheet here. (D) Outflows at the position of the current sheet. (E) Projection-corrected images of the flare ribbons observed in AIA 1600 Å. The letter P denotes the positive ribbon and N denotes the negative ribbon. (F) Evolution of the bottom QSL of our simulation, where  $\text{sgn}(B_z)$  denotes the sign of  $B_z$ . The letter P denotes the positive QSL and N denotes the negative QSL. The slices in C and D are located at the position labeled by the white solid line in the first panel of Figure 3(A). Row A is shown at panel *a*, and rows C and D are shown at panel *c* and panel *d* in the animation of Figure 2, respectively. The QSL evolution in row F is shown in panel *b*.



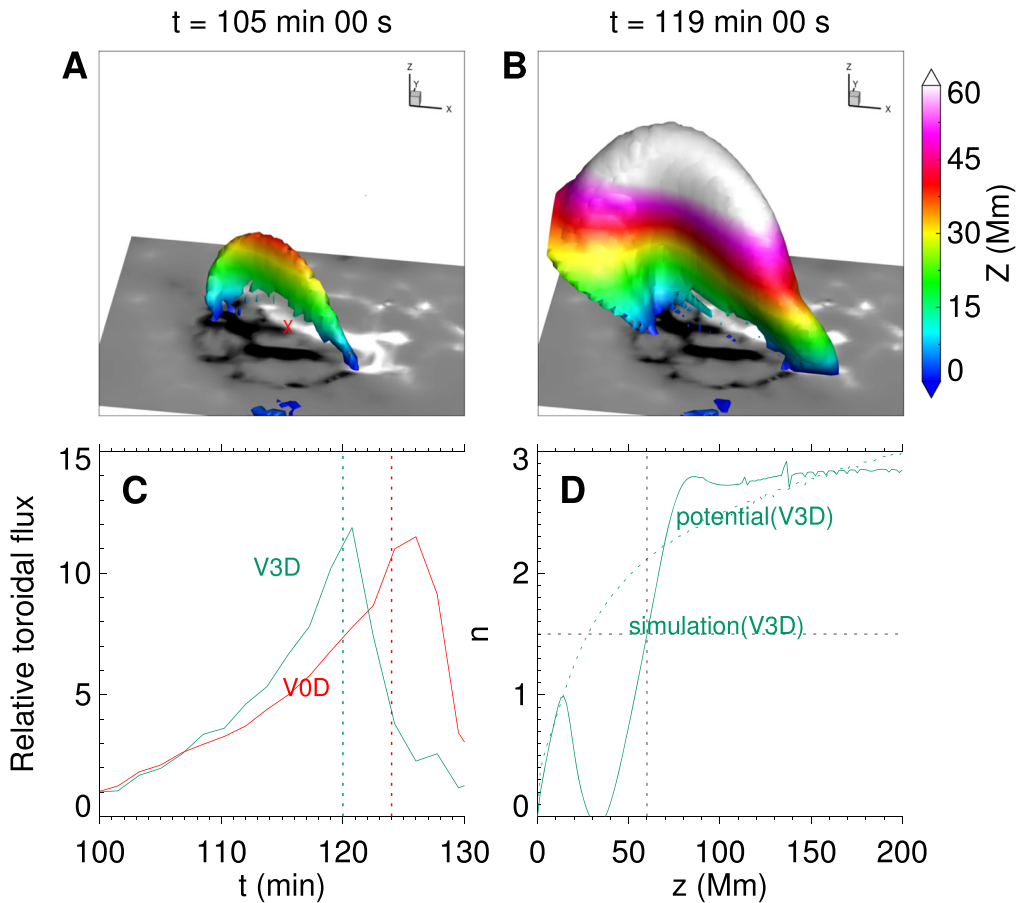


**Figure 5.** (A) The isosurface of  $T_w = -1$  and  $T_w$  is the twist number of the magnetic field in the “V3D” simulation. The red “X” labels the position where we calculate the decay index. (B) Same as A but at a different time. (C) The green solid curve denotes the relative toroidal flux of the MFR in the “V3D” simulation, and the red solid curve in the “V0D” simulation with both curves normalized by their initial values, respectively. The two vertical dashed lines in different colors denote the onset time of the “V0D” and “V3D” simulations, respectively. The toroidal flux is defined as  $\int_s B_z ds$ , where “s” is the region of  $T_w < -1$  and  $B_z < 0$  at the bottom boundary. (D) The decay index  $n$  of the magnetic field in the “V3D” simulation (solid curve), and the corresponding potential field (dashed curve) at the same time of  $t = 119$  minutes. The horizontal dashed line denotes the critical value of  $n = 1.5$ , and the vertical dashed line denotes the critical height, above which  $n > 1.5$ .

allowed slow reconnection (i.e., a slow dissipation of the current) to take place without impulsive energy release (i.e., not a Pescheck-type reconnection, Yokoyama & Shibata 1994). The eruption of this “V0D” run has a similar onset time and strength to the “V3D” run, which further indicates that after  $t = 100$  minutes in the “V3D” run, the velocity field on the bottom boundary is not necessary and the instability is sufficient to trigger the eruption. It follows the basic development stage of TI, i.e., the rising MFR stretched the overlying field, and consequently, the flare CS formed below the MFR. Since we did not use any explicit value of magnetic resistivity, and since the CS formed in a dynamic way, the width of the CS could become very thin to trigger the fast reconnection easily as pointed out by Jiang et al. (2021b), further driving the eruption. Based on the analysis of our simulation and the supplementary numerical experiment (“V0D” simulation), along with the consistency between our simulation results and observations that have been shown above, we conclude that TI is the initiation mechanism of the X1.1 flare in AR 11429 on 2012 March 5.

#### 4. Conclusions and Discussions

We carried out a full 3D MHD simulation of an X-class flare eruption event on 2012 March 5 in AR 11429 using the V-driven DARE-MHD model. An MHD equilibrium was

obtained by relaxing the NLFFF reconstructed by the CESE-MHD-NLFFF code and was set as the initial condition. Then, the initial state was driven to evolve by the DAVE4VM velocity field on the bottom boundary of our simulation box. The analysis of the quasi-static evolution stage before the eruption onset shows the gradual formation of an MFR above the main PIL. When the MFR first appeared, it was relatively low and then it grew into the torus-unstable region, after which TI was triggered. Then the energy conversion process was accomplished by reconnection in the CS that is formed due to the stretching effect of the erupting MFR. The images from the SDO observation and the important physical quantities computed from the magnetograms are reasonably consistent with our result in the preflare magnetic structure, the morphology of flare ribbons, evolution curves of the magnetic and kinetic energies, as well as the total unsigned magnetic flux. The time duration of the quasi-static evolution process before the simulated eruption is also very close to the actual timescale before the flare onset.




Nevertheless, our simulation does not reproduce accurately the evolution of the magnetic field as shown in the observed magnetograms. As can be seen in the last panel of Figure 3(A), part of the magnetic flux was transported to and concentrated at the edge of the AR, while this pileup was not observed in HMI magnetograms. One likely reason for this flux pileup is that the

DAVE4VM method only solves the normal component of the magnetic induction equation in the least-squares sense (Lumme et al. 2019), which may not reproduce the velocity precisely at every point and can only be used to approximate the overall distribution and evolution of magnetic flux in the AR. In addition, the magnetic flux on the photosphere should be dispersed and dissipated by granular and supergranular convection (Wang et al. 1989) as well as small-scale turbulent diffusion in practical situations. Therefore, without dealing properly with these effects, the flux pileup will be more obvious than in observations, and as a result, the magnetic energy injection rate of the “V3D” run will be overall higher than the “OB” one as shown in Figure 2(A) (comparing the black dashed line and the black solid line). This unrealistic flux pileup may also contribute to the overshoot of the magnetic energy increase (Figure 2(A), the mismatch of the black dashed line, and the green line before the eruption) because it results in a very large magnetic gradient at the bottom boundary, thus even the finest spatial resolution in our simulation was inadequate to capture the too high gradient during the time duration close to the eruption onset (i.e.,  $t \in [97, 122]$  minutes). The insufficient grid resolution led to considerable numerical error there, which thus makes the magnetic energy increase higher than the magnetic energy injection in the “V3D” simulation. Proper settings of the numerical diffusion and grid resolution, along with improved methods for deriving the photospheric flow, will need to be considered in future works for a more accurate data-driven simulation of solar eruptions.

To summarize, our simulation shows that, besides inputting the time series of the vector magnetogram, the numerical model of the solar corona can be driven to erupt by inputting the time-series velocity field at the bottom boundary, in which the driver, i.e., the bottom velocity field, is derived from the time series of vector magnetograms. The numerical model we established here shows the possibility of driving the evolution of solar corona using different physical variables, which offers a straightforward way to reveal the eruption mechanisms in real events. Thus, such a model has great potential in forecasting the onset time as well as the strength of solar eruptions and evaluating the quantitative impact on space weather.

This work is jointly supported by the National Natural Science Foundation of China (NSFC 41731067, 42030204, 42174200), the Fundamental Research Funds for the Central Universities (grant No. HIT.OCEF.2021033), and Shenzhen Science and Technology Program (grant Nos. RCJC20210609104422048 and JCYJ20190806142609035). The computational work was carried out on TianHe-1(A), National Supercomputer Center in Tianjin, China, and we thank Jun Chen for his informative and helpful discussions.

## ORCID iDs

Xinyi Wang  <https://orcid.org/0000-0002-2565-2246>  
 Chaowei Jiang  <https://orcid.org/0000-0002-7018-6862>  
 Xueshang Feng  <https://orcid.org/0000-0001-8605-2159>

## References

- Antiochos, S. K., DeVore, C. R., & Klimchuk, J. A. 1999, *ApJ*, 510, 485  
 Berger, M. A., & Prior, C. 2006, *JPhA*, 39, 8321  
 Bobra, M. G., Sun, X., Hoeksema, J. T., et al. 2014, *SoPh*, 289, 3549  
 Chen, P. F. 2011, *LRSF*, 8, 1  
 Cheng, X., Guo, Y., & Ding, M. 2017, *ScChD*, 60, 1383  
 Cheung, M. C. M., & DeRosa, M. L. 2012, *ApJ*, 757, 147  
 Chintzoglou, G., Patsourakos, S., & Vourlidas, A. 2015, *ApJ*, 809, 34  
 Dhakal, S. K., Chintzoglou, G., & Zhang, J. 2018, *ApJ*, 860, 35  
 Dhakal, S. K., Zhang, J., Vemareddy, P., & Karna, N. 2020, *ApJ*, 901, 40  
 Duan, A., Jiang, C., He, W., et al. 2019, *ApJ*, 884, 73  
 Fisher, G. H., Kazachenko, M. D., & Welsch, B. T., et al. 2020, *ApJS*, 248, 2  
 Fisher, G. H., Welsch, B. T., & Abbett, W. P. 2012, *SoPh*, 277, 153  
 Fisher, G. H., Welsch, B. T., Abbett, W. P., & Bercik, D. J. 2010, *ApJ*, 715, 242  
 Fisher, G. H., Abbett, W. P., Bercik, D. J., et al. 2015, *SpWea*, 13, 369  
 Forbes, T. G. 2000, *JGR*, 105, 23153  
 Guo, Y., Xia, C., Keppens, R., Ding, M. D., & Chen, P. F. 2019, *ApJL*, 870, L21  
 Hayashi, K., Feng, X., Xiong, M., & Jiang, C. 2018, *ApJ*, 855, 11  
 Hayashi, K., Feng, X., Xiong, M., & Jiang, C. 2019, *ApJL*, 871, L28  
 He, W., Jiang, C., Zou, P., et al. 2020, *ApJ*, 892, 9  
 Jiang, C. 2022, *Reviews of Geophysics and Planetary Physics*, 53, 497  
 Jiang, C., Bian, X., Sun, T., & Feng, X. 2021a, *FrP*, 9, 224  
 Jiang, C., Feng, X., Liu, R., et al. 2021b, *NatAs*, 5, 1126  
 Jiang, C., & Feng, X. 2012, *ApJ*, 749, 135  
 Jiang, C., & Feng, X. 2013, *ApJ*, 769, 144  
 Jiang, C., Feng, X., Guo, Y., & Hu, Q. 2022, *Innov*, 3, 100236  
 Jiang, C., Feng, X., Zhang, J., & Zhong, D. 2010, *SoPh*, 267, 463  
 Jiang, C., Wu, S. T., Feng, X., & Hu, Q. 2016, *NatCo*, 7, 11522  
 Jiang, C., Zou, P., Feng, X., et al. 2018, *ApJ*, 869, 13  
 Kaneko, T., Park, S.-H., & Kusano, K. 2021, *ApJ*, 909, 155  
 Lemen, J. R., Title, A. M., Akin, D. J., et al. 2012, *SoPh*, 275, 17  
 Lin, J., & Forbes, T. G. 2000, *JGR*, 105, 2375  
 Liu, C., Chen, T., & Zhao, X. 2019, *A&A*, 626, A91  
 Liu, R., Kliem, B., Titov, V. S., et al. 2016, *ApJ*, 818, 148  
 Lumme, E., Kazachenko, M. D., Fisher, G. H., et al. 2019, *SoPh*, 294, 84  
 Moore, R. L., & Labonte, B. J. 1980, in *IAU Symp. 91, Solar and Interplanetary Dynamics*, ed. M. Dryer (Cambridge: Cambridge Univ. Press), 207  
 Moore, R. L., & Roumeliotis, G. 1992, *Eruptive Solar Flares* ed. Z. Svestka, B. V. Jackson, & M. E. Machado, Vol. 399 (Berlin: Springer), 69  
 Pomoell, J., Lumme, E., & Kilpua, E. 2019, *SoPh*, 294, 41  
 Price, D. J., Pomoell, J., Lumme, E., & Kilpua, E. K. J. 2019, *A&A*, 628, A114  
 Priest, E. 2014, *Magnetohydrodynamics of the Sun* (Cambridge: Cambridge Univ. Press)  
 Schmieder, B., Démoulin, P., & Aulanier, G. 2013, *AdSpR*, 51, 1967  
 Schou, J., Scherrer, P. H., Bush, R. I., et al. 2012, *SoPh*, 275, 229  
 Schuck, P. W. 2008, *ApJ*, 683, 1134  
 Shimizu, T., Lites, B. W., & Bamba, Y. 2014, *PASJ*, 66, S14  
 Titov, V. S., Hornig, G., & Démoulin, P. 2002, *JGRA*, 107, 1164  
 Wang, Y. M., Nash, A. G., & Sheeley, N. R. 1989, *Sci*, 245, 712  
 Yokoyama, T., & Shibata, K. 1994, *ApJL*, 436, L197  
 Zhang, Y., Bastian, T. S., Liu, J. H., et al. 2021, *ApJ*, 910, 40  
 Zheng, J.-C., Yang, Z.-L., Guo, J.-P., et al. 2017, *RAA*, 17, 081  
 Zhong, Z., Guo, Y., & Ding, M. D. 2021, *NatCo*, 12, 2734